Contents lists available at ScienceDirect

Transactions of Nonferrous Metals Society of China

36(2026) 507−521

www.tnmsc.cn

Morphological and size evolution of γ' phases during aging in nickel-based single crystal superalloy

Ye-yuan HU, Shao-xiang LI, Qing-yan XU*

Key Laboratory for Advanced Materials Processing Technology, Ministry of Education, School of Materials Science and Engineering, Tsinghua University, Beijing 100084, China

Abstract: A multistage solution treatment process was applied for nickel-based single crystal superalloys, complemented by various aging durations and cooling rates. The microstructure was characterized by scanning electron microscopy (SEM) to observe the γ' phase. Additionally, phase field simulations were conducted to model the growth of γ' precipitates during aging and analyze their morphological evolution. The experimental results demonstrated that the multistage solution treatment effectively eliminated eutectic phases and carbides. Moreover, samples aged for 10 min exhibited larger and more rectangular γ' precipitates compared with those aged for 5 min. Notably, secondary γ' precipitates were observed in samples subjected to water cooling. Two indices for quantifying rectangularization were proposed and successfully applied. Based on the simulation results, lattice mismatch induced coherency stresses and elevated stress triaxiality along the ⟨111⟩ direction contributed to the rectangularization of the γ' phase.

Keywords: nickel-based superalloy; aging holding time; γ' rectangularization; phase field simulation

1 Introduction

Nickel-based single crystal (SC) superalloys have earned a pivotal role in aerospace engineering, particularly in producing high-performance turbine blades used in aeronautical engines [1−3]. However, the as-cast state of SC superalloys may exhibit mechanical weakness due to the presence of eutectic phases and carbides, which creates challenges for their practical use. Consequently, heat treatment plays a crucial role in addressing these deficiencies and improving the alloy's mechanical performance [4−6]. The conventional heat treatment process involves a sequential solution treatment followed by a two-stage aging process, widely adopted in nickel-based single crystal superalloys [7−9]. The primary objectives of the solution treatment are to dissolve unwanted eutectic phases and carbides as thoroughly as possible and to achieve an optimal supersaturated solid solution. The subsequent two-stage aging process facilitates the formation of neatly arranged γ' precipitates, significantly enhancing the service performance of alloy [10−12]. Understanding the influence of temperature and holding time during these treatment stages is crucial, as they significantly impact the microstructural evolution and, consequently, the mechanical properties of nickel-based single crystal superalloys [13−16].

Recent investigations have highlighted the advantages of using elevated solution treatment temperatures during solid solution processing to mitigate compositional segregation [17−19]. It is generally believed that, while avoiding initial melting, high solution treatment temperatures lead to improved service performance. The "solutioning window", between the γ' solvus temperature and the

Corresponding author: *Qing-yan XU, Tel: +86-10-62795482, E-mail: scjxqy@tsinghua.edu.cn
https://doi.org/10.1016/S1003-6326(25)66978-0
Received 9 May 2024; accepted 20 January 2025
1003-6326/© 2026 The Nonferrous Metals Society of China. Published by Elsevier Ltd & Science Press
This is an open access article under the CC BY-NC-ND license (http://creativecommons.org/licenses/by-nc-nd/4.0/)

initial melting temperature, is critical in providing sufficient opportunities for dissolving undesirable phases. To expand this "solutioning window", researchers have introduced multistage solution heat treatments that raise the initial melting temperature, effectively broadening the range for the dissolution of unfavorable phases. HEGDE et al [20] used stepwise homogenization solution heat treatments and found that steps below the γ' solvus temperature stabilized the eutectic phase, while steps above the γ' solvus temperature improved the homogenization and reduced the eutectic phase fraction. LV [21] applied several stepwise solution heat treatments to DD5 superalloy, which are (1280 °C, 2 h) + (1315 °C, 2 h) + (1320 °C, 2 h) + (1325 °C, 6 h). AC solution route produced a favorable microstructure. In addition to the aforementioned stepwise solution heat treatments, innovative techniques such as ramp solution heat treatment [22] and remelting solution treatment [9] have emerged in recent years. ZHANG et al [22] proposed a ramp solution heat treatment at a higher permissible temperature, which efficiently reduced residual segregations. CHENG et al [9] utilized a remelting heat treatment to achieve superior element homogenization. These methods have effectively reduced elemental segregation and prepared an optimal microstructure for subsequent aging treatments.

Along with appropriate solution treatment, choosing befitting aging treatment is of great importance as well. The primary aging stage aims to achieve appropriately sized and uniformly distributed γ' precipitates, while the secondary aging stage focuses on enhancing the cubic morphology and optimizing the volume fraction of the γ' precipitates [23,24]. WEI et al [25] explored the influence of temperature and holding time during primary aging treatment on the size and volume fraction of γ' phase. Their findings showed that with an increase in aging temperature or time, the size and volume fraction of γ' precipitates increased, and the morphology of the γ' precipitates gradually changed from cubic shape to rod shape. However, it was observed that the changes induced by aging time were less pronounced than those caused by change of aging temperature, whether in terms of size, shape, or volume fraction [26,27]. Similarly, XU et al [28] concluded that elevating the temperature was much more effective than prolonging the time in terms of controlling size. QU et al [29] designed cooling and remelting processes after aging to explore the formation of secondary γ' phases and confirmed that they were likely to precipitate at temperatures between 950 and 1000 °C. XIA et al [30] applied rapid liquid-nitrogen quenching following aging treatment, which promoted extensive nucleation of ultrafine γ' particles. However, there is currently a lack of quantitative descriptions considering the morphological changes of the γ' phase during aging. Furthermore, although applying various cooling rates following solution treatment is regarded as a contributing factor to the distinct morphological characteristics of primary and secondary γ' precipitates [9,31], systematic research on the effect of cooling rate after aging treatment is still scarce.

Various experimental researches have explored heat treatment processes, and the phase field method has also been applied to studying the nucleation and growth of γ' phases. YANG et al [32] explored the influence of cooling rate (after the first aging stage) on the evolution of primary and secondary γ' precipitates using phase field simulation. Similarly, XU et al [33] conducted simulations of precipitation and growth of γ' phase in DD6 superalloy using the multiphase-field method and an explicit nucleation algorithm. Phase field simulation proves to be an effective tool for investigating the underlying mechanisms responsible for the alteration in size and shape of the γ' phases.

In summary, further exploration of γ' phase changes during aging is still warranted, focusing on quantitative studies on the effect of aging duration on the morphology of the γ' phase, mechanistic explanations for the changes in size and morphology of the γ' phase, and the influence of cooling rates after aging on the microstructure of the superalloy.

This study adopted a comprehensive approach, implementing multistage solution treatment alongside aging treatments with varying holding time and cooling rates on a secondary generation nickel-based single crystal superalloy. The main objects focused on quantitatively studying the changes in γ' size and morphology over time and understanding the processes of primary and secondary γ' precipitation. Two indices for quantifying the rectangularity of the γ' phase were proposed and compared. Additionally, phase field simulation was employed to illustrate the

morphology change of the γ' phase during aging.

2 Experimental

2.1 Material and heat treatment

The nominal chemical composition of DD5 superalloy used in this study is listed in Table 1. An alloy ingot was fabricated using vacuum induction melting. It was then directionally solidified in a furnace to form an as-cast single crystal rod with a diameter of 16 mm and a length of 200 mm. The as-cast DD5 superalloy was subsequently machined into samples with dimensions of d10 mm × 15 mm for heat treatment experiments. The sample for microstructure characterization is illustrated in Fig. 1. We selected the middle part of the heat-treated samples (the orange section in Fig. 1) for the characterization experiments. A schematic diagram of the heat treatment process used in this study is shown in Fig. 2. The as-cast samples were solution-treated at (1280 °C, 2 h) + (1315 °C, 2 h) + (1320 °C, 2 h) + (1325 °C, 6 h) in a box furnace and then air cooled. Subsequently, the solution-treated samples were subjected to the following aging process. Solution-treated samples were aged at 1100 °C for 5 or 10 min in a Gleeble−3500 thermal simulator, with five different cooling strategies (25, 50, 100 and 125 °C/min, and water cooling).

Table 1 Nominal chemical composition of DD5 single crystal superalloy (wt.%)

Al	Co	Cr	Mo	W	Re	Ta	Hf	Ni
6.2	7.5	7.0	1.5	5.0	3.0	6.5	0.15	Bal.

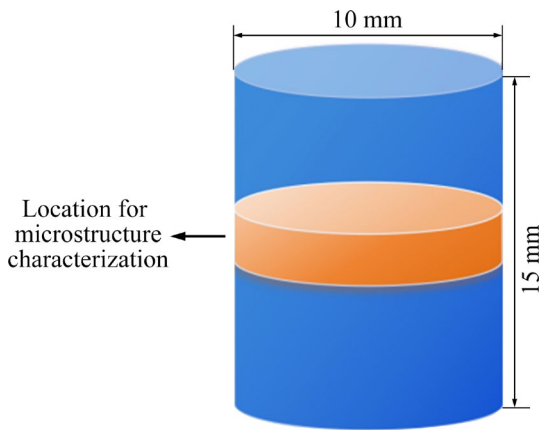

Fig. 1 Schematic diagram of sample size and selected location for microstructure characterization

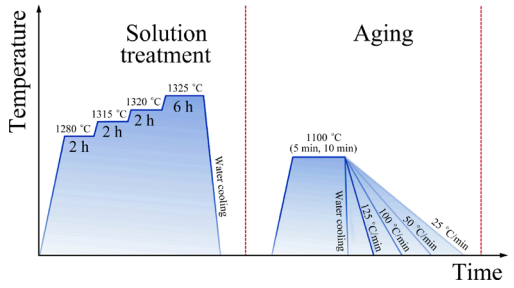

Fig. 2 Schematic diagram of heat treatment operated in this study

2.2 Microstructure characterization

Common microstructure observations were performed by optical microscopy (OM) and field emission scanning electron microscope (SEM) Zeiss GEMINISEM 500 at 20 kV. SEM samples were prepared through an etching process in a solution of 5 g $CuSO_4$, 100 mL HCl, 5 mL H_2SO_4, and 80 mL H_2O.

Due to the lack of a quantified indicator for rectangularity in previous studies, two indices were proposed in this study: roundness (R) and curvature derivative range (CDR). Roundness is calculated using $R=c^2/(4\pi S)$, where c is the perimeter, and S is the area. The concept of CDR is based on the variation of curvature and its derivative along the γ' phase contour. To calculate CDR, the curvature at each point along the γ' phase contour is first determined, followed by the calculation of the curvature derivative. The value of CDR is then obtained by subtracting the minimum from the maximum curvature derivative within the segment of the curve. A larger CDR indicates a higher degree of rectangularization. CDR was calculated for more than 30 segments for each experimental condition, and the average was taken to obtain the overall CDR for the γ' phase under that condition. The pixel analysis function and measurement tools of Image J software were used to quantify the size, roundness, and curvature of γ' precipitates in heat-treated material, based on the obtained SEM images, as well as for the simulated γ' precipitates. For representative statistics, at least 100 particles were counted from each micrograph, and three micrographs taken from different dendrite stem areas were analyzed.

2.3 Phase field model for γ' growth during aging

A phase field simulation was applied in this study. The mixture concentration ($\vec{c}$) was defined.

The phase field variable (ϕ) during aging is illustrated in Fig. 3. When the ϕ is 0, it represents the γ phase, while it represents the γ' phase when it is 1.

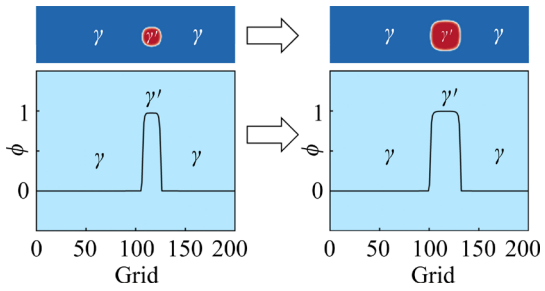

Fig. 3 Schematic diagram of phase field variable change during aging

The concentration field is represented by $\vec{c}(\vec{x},t)$, which means that the composition field variables change with position $\vec{x}$ and time t in different phases. Utilizing the phase composition field $\{\vec{c}_\alpha(\vec{x},t)\}$, the concentration field can be interpolated as follows:

$$\vec{c}=\sum_{\alpha}\phi_\alpha\vec{c}_\alpha \tag{1}$$

The total energy (F) within the calculation domain (Ω) is obtained through the integration of energy density functions, which can be divided into interfacial energy density f^{GB}, chemical free energy density f^{CH}, and elastic energy density f^{EL} [34]:

$$F=\int_\Omega f^{\mathrm{GB}}+f^{\mathrm{CH}}+f^{\mathrm{EL}} \tag{2}$$

The interfacial energy density is calculated by Eq. (3) [34]:

$$f^{\mathrm{GB}}=\kappa_{\alpha\beta}/\eta_{\alpha\beta}\left\{(\eta_{\alpha\beta}^2/\pi^2)\cdot\left|\nabla\phi_\alpha\cdot\nabla\phi_\beta\right|+W_{\alpha\beta}\right\} \tag{3}$$

$$W_{\alpha\beta}=\phi_\alpha\phi_\beta \tag{4}$$

where $\kappa_{\alpha\beta}$ refers to the interfacial energy between α and β phases, and $\eta_{\alpha\beta}$ represents the interface width, here, it is denoted as η.

The chemical free energy density is calculated by Eq. (5) [34]:

$$f^{\mathrm{CH}}=\sum_{\alpha=0}^{\nu}\phi_\alpha f_\alpha(\vec{c}_\alpha)+\vec{\mu}\left(\vec{c}-\sum_{\alpha=1}^{N}\phi_\alpha\vec{c}_\alpha\right) \tag{5}$$

where $f_\alpha(\vec{c}_\alpha)$ is the volume free energy for each phase, and $\vec{\mu}=\partial f^{\mathrm{CH}}/\partial\vec{c}$ represents the chemical potential vector. And elastic energy density can be calculated as follows [34]:

$$f^{\mathrm{EL}}=1/2\varepsilon_{ij}^{\mathrm{el}}C_{ijkl}\varepsilon_{kl}^{\mathrm{el}} \tag{6}$$

The elastic ($\varepsilon_{kl}^{\mathrm{el}}$) strain is given by [25]

$$\varepsilon_{ij}^{\mathrm{el}}=\varepsilon_{ij}-\varepsilon_{ij}^{*} \tag{7}$$

where ε_{ij} and ε_{ij}^{*} are the total strain and equivalent eigenstrain induced by lattice mismatch, respectively. The C_{ijkl} denotes the effective elastic constants, where i, j, k and l, respectively represent the indices of the elastic tensor, and the interpolation form of the Reuss limit is used [35,36].

The local stress field (σ_{ij}) is calculated using Eq. (8), and it is assumed to be equal for different phases at the interface:

$$\sigma_{ij}=\delta F/\delta\varepsilon_{ij}=C_{ijkl}\varepsilon_{ij}^{\mathrm{el}} \tag{8}$$

The evolution of the phase field and concentration field is determined by solving the time-dependent Ginzburg−Landau equation [37] and the Cahn−Hilliard nonlinear diffusion equation [38]:

$$\partial\phi_\alpha/\partial t=-(\tilde{M}_{\alpha\beta}/\nu)\left(\delta F/\delta\phi_\alpha-\delta F/\delta\phi_\beta\right) \tag{9}$$

$$\partial\vec{c}/\partial t=\nabla\left(\sum_{\alpha=0}^{\nu}D_\alpha^i\phi_\alpha\nabla c_\alpha^i\right) \tag{10}$$

where $\tilde{M}_{\alpha\beta}$ represents the interface mobility, and D_α^i is the chemical mobility of element i in α phase. The final form of Eq. (9) is given by [34]

$$\partial\phi_\alpha/\partial t=(M_{\alpha\beta}/\nu)\cdot\left\{\sum_{p=0}^{\nu}\left(\kappa_{\beta p}-\kappa_{\alpha p}\right)I_p+\pi^2/(8\eta)(\Delta G_{\alpha\beta}^{\mathrm{CH}}+\Delta G_{\alpha\beta}^{\mathrm{EL}})\right\} \tag{11}$$

$$I_p=\nabla^2\phi_p+(\pi^2/\eta^2)\phi_p \tag{12}$$

where ν is the total number of phases, and ϕ_p is the phase field variable of p phase. In this study, ν equals 2, corresponding to the γ phase and the γ' phase. $M_{\alpha\beta}=\tilde{M}_{\alpha\beta}\cdot 8\eta/\pi^2$, and the chemical driving force $\Delta G_{\alpha\beta}^{\mathrm{CH}}$ can be obtained by solving Eqs. (13) and (14) [39,40]:

$$\Delta G_{\alpha\beta}^{\mathrm{CH}}\approx\sum_{i=1}^{n}\partial\Delta G_{\alpha\beta}^{\mathrm{CH}}/\partial c_\alpha^i(c_\alpha^i-c_\alpha^{i,\mathrm{eq}}) \tag{13}$$

$$\partial\Delta G_{\alpha\beta}^{\mathrm{CH}}/\partial c_\alpha^i\approx-\sum_{k=1}^{n-1}\left(T_\alpha^{ki}-T_\alpha^{ni}\right)\left(c_\beta^i-c_\alpha^i\right) \tag{14}$$

where $c_\alpha^{i,\mathrm{eq}}$ is the equilibrium concentration of element i in the α phase, and $T_\alpha^{ki}=\partial\mu_\alpha^k/\partial c_\alpha^i$ is the thermodynamic factor, which can be calculated from the commercial thermodynamic database PanNickel©. The elastic driving force $\Delta G_{\alpha\beta}^{\mathrm{EL}}$ is calculated using Eq. (15) [41]:

$$\Delta G_{\alpha\beta}^{\mathrm{EL}}=\sigma_{kl}\left\{\left(\varepsilon_{\alpha,kl}^{*}-\varepsilon_{\beta,kl}^{*}\right)-\frac{1}{2}[(C_{klnm}^{\alpha})^{-1}-(C_{klnm}^{\beta})^{-1}]\sigma_{mn}\right\} \tag{15}$$

where $\varepsilon_{\alpha,kl}^{*}$ and $\varepsilon_{\beta,kl}^{*}$ are the Eigen strains for phases α and β respectively, C_{klnm}^{α} and C_{klnm}^{β} are the elastic constants of phases α and β respectively, σ_{kl} and σ_{mn} are the components of the local stress tensor.

To obtain the elastic driving force $\Delta G_{\alpha\beta}^{\mathrm{EL}}$, it is necessary to solve the mechanical equilibrium within the calculation domain Ω:

$$\partial\sigma_{ij}/\partial x_j=0 \tag{16}$$

The stress control method in Ref. [42] can convert stress boundary conditions into strain boundary conditions, facilitating the solution of mechanical problems. Assuming the entire calculation domain is a homogeneous system, the elastic stress must satisfy the condition of equal average stress in the region to the external load, as shown in Eq. (17):

$$\langle\sigma_{ij}\rangle=1/V\int_{\Omega}\sigma_{ij}\mathrm{d}\Omega=\sigma_{ij}^{\mathrm{appl}} \tag{17}$$

where $\langle\cdot\rangle=1/V\int_{\Omega}\mathrm{d}\Omega$, V represents the volume of the computational domain. For two-dimensional calculations, V corresponds to the area of the computational domain. Define $S_{ijkl}=\left(\left\langle C_{ijkl}\right\rangle\right)^{-1}$. Using Eqs. (18) and (19) iteratively, the stress boundary conditions can be transformed into strain boundary conditions. This transformation allows solving the mechanical equilibrium through the classical fast Fourier transform (FFT) method [42].

$$\overline{\varepsilon}_{ij}^{0}=S_{ijkl}:\sigma_{ij}^{\mathrm{appl}} \tag{18}$$

$$\overline{\varepsilon}_{ij}^{n+1}=\overline{\varepsilon}_{ij}^{n}+S_{ijkl}:\left(\sigma_{ij}^{\mathrm{appl}}-\langle\sigma_{ij}\rangle\right) \tag{19}$$

Besides, the diffusion of elements may have a non-negligible effect on the lattice parameters of γ' and γ phase. As reported by NEUMEIER et al [43], the theoretical lattice parameters of the γ phase, a^{γ}, and the γ' phase, $a^{\gamma'}$, are determined as a function of temperature according to the following equations, and the Hf element is not considered for its low concentration.

$$\begin{aligned}a^{\gamma}=&3.524+0.187c_{\mathrm{Al}}^{\gamma}+0.021c_{\mathrm{Co}}^{\gamma}+0.119c_{\mathrm{Cr}}^{\gamma}+\\&0.461c_{\mathrm{Mo}}^{\gamma}+0.439c_{\mathrm{Re}}^{\gamma}+0.687c_{\mathrm{Ta}}^{\gamma}+0.432c_{\mathrm{W}}^{\gamma}+\\&4.077\times10^{-5}T+1.499\times10^{-8}T^{2}\end{aligned} \tag{20}$$

$$\begin{aligned}a^{\gamma'}=&3.57-0.003c_{\mathrm{Co}}^{\gamma'}-0.003c_{\mathrm{Cr}}^{\gamma'}+0.22c_{\mathrm{Mo}}^{\gamma'}+\\&0.262c_{\mathrm{Re}}^{\gamma'}+0.491c_{\mathrm{Ta}}^{\gamma'}+0.194\cdot c_{\mathrm{W}}^{\gamma'}+\\&4.197\times10^{-5}T+1.17\times10^{-8}T^{2}\end{aligned} \tag{21}$$

The simulation program was developed by ourselves and compiled by C++ programming to realize the multi-phase field simulation. The simulation parameters were calculated by Thermo-Calc and Pandat software. All the simulations have periodic boundary conditions and the same meshing conditions. The calculation domain is discretized into 400×400 grids.

3 Results and discussion

3.1 Effects of multistage solution treatment on microstructure

The multistage solution treatment plays a critical role in refining the microstructure of the DD5 superalloy. A comparison of the dendritic structures of the as-cast and solution-treated DD5 superalloy reveals significant differences, as shown in Fig. 4. The as-cast sample exhibits prominent dendrites, indicating elemental segregation between the dendritic and interdendritic regions. Notably, there are discernible eutectic phases in the as-cast samples. However, after the solution heat treatment, a remarkable transformation appears. The solution treatment leads to the dissolution of carbides and nearly complete eradication of the eutectic phases.

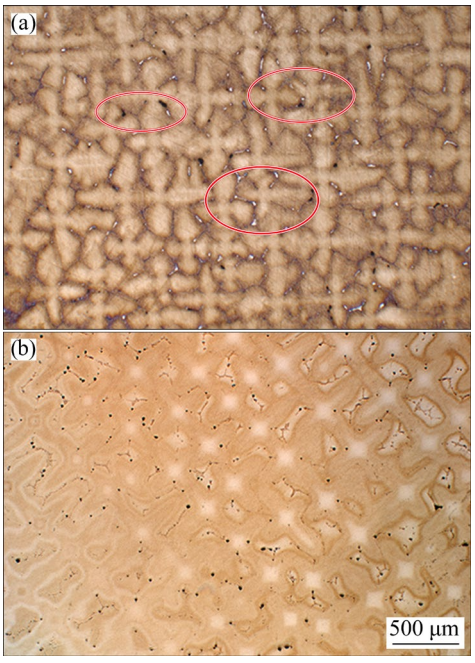

Fig. 4 Morphology of dendritic structure in as-cast (a) and solution-treated (b) DD5 superalloy

This significant change from the as-cast state indicates the effectiveness of the solution treatment in purifying the microstructure of alloy.

The DD5 superalloy has a narrow "solutioning window" due to its initial melting temperature of 1310−1315 °C. This presents challenges in achieving effective solubility during solution treatments [21]. To overcome this limitation, the initial melting temperature was increased after homogenization at 1280 °C, thereby widening the "solutioning window." Subsequent multistage solution treatments further expanded this window, creating more favorable conditions for the solution process. Higher solution temperatures and longer treatment time accelerate diffusion, leading to more effective dissolution of eutectic phases and carbides [44]. Despite the significant dissolution, residual micropores remain in the solution-treated sample, indicating areas that may require further optimization in the solution treatment process.

Figure 5 presents a comparative visualization of the γ' precipitates in the as-cast and solution-treated DD5 superalloy samples. In the as-cast sample, the γ' precipitates exhibit a coarse structure arranged in a distinctive butterfly-like pattern. In contrast, the solution-treated samples show a very different structure. The precipitates are densely packed and significantly refined, indicating a substantial transformation following the solution treatment. The nucleation of γ' precipitates primarily occurs during the cooling phase after the solution treatment. This phenomenon is attributed to the high concentration of supersaturated solute elements within the γ matrix, significantly enhancing the nucleation process [28].

3.2 Effects of cooling rate after aging on secondary γ' precipitates

Figure 6 shows a comprehensive depiction of the morphology of γ' precipitates after different aging treatments. Figure 6(a) shows the morphology after the solution treatment, while Figs. 6(b−f) illustrate the diverse morphologies resulting from aging treatments for 5 min at different cooling rates. Correspondingly, Fig. 7 presents the size distribution

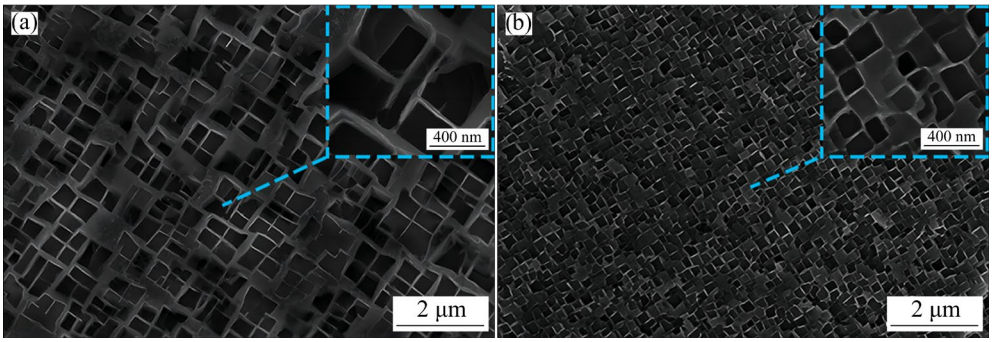

Fig. 5 Morphology of γ' precipitates in as-cast (a) and solution-treated (b) DD5 superalloy

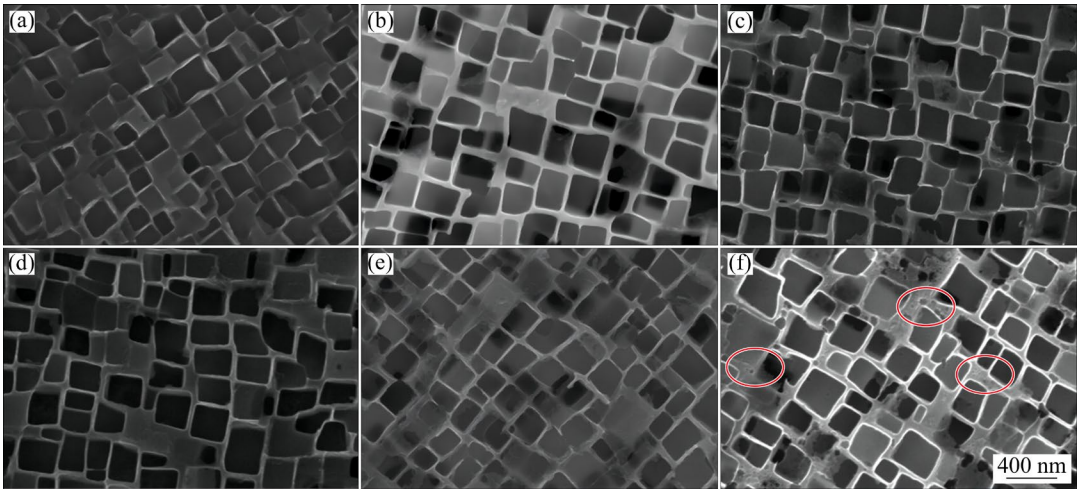

Fig. 6 Morphology of γ' precipitates after solution treatment (a), and after aging treatment for 5 min at different cooling rates: (b) 25 °C/min; (c) 50 °C/min; (d) 100 °C/min; (e) 125 °C/min; (f) Water cooling

of the γ' precipitates for the samples in Fig. 6. The black line in the figure represents the cumulative frequency of the size distribution. The results show that after aging for 5 min with different cooling rates, the γ' precipitates are larger than those in the solution-treated samples. Interestingly, only marginal differences in the size of the γ' precipitates are observed among the five aging conditions. This phenomenon arises due to the initial presence of closely arranged precipitates in the solution-treated sample, which further facilitates precipitate growth during subsequent aging [27].

Notably, among the samples subjected to different cooling rates, only the sample subjected to water cooling shows secondary γ' precipitates, as indicated by red circles in Figs. 6(f) and 8(f). Under isothermal conditions or very slow cooling rates, the formation of secondary precipitates is inhibited, as studied in Ref. [33]. This inhibition leads to the occurrence of a "soft impingement" phenomenon, where the level of supersaturation gradually decreases, reducing the nucleation rate. This phenomenon, in which element diffusion lowers supersaturation and subsequently decreases nucleation, is commonly referred to as "soft impingement" [45,46].

Under conditions characterized by intermediate cooling rates, a bimodal microstructure emerges, driven by the interplay between undercooling and

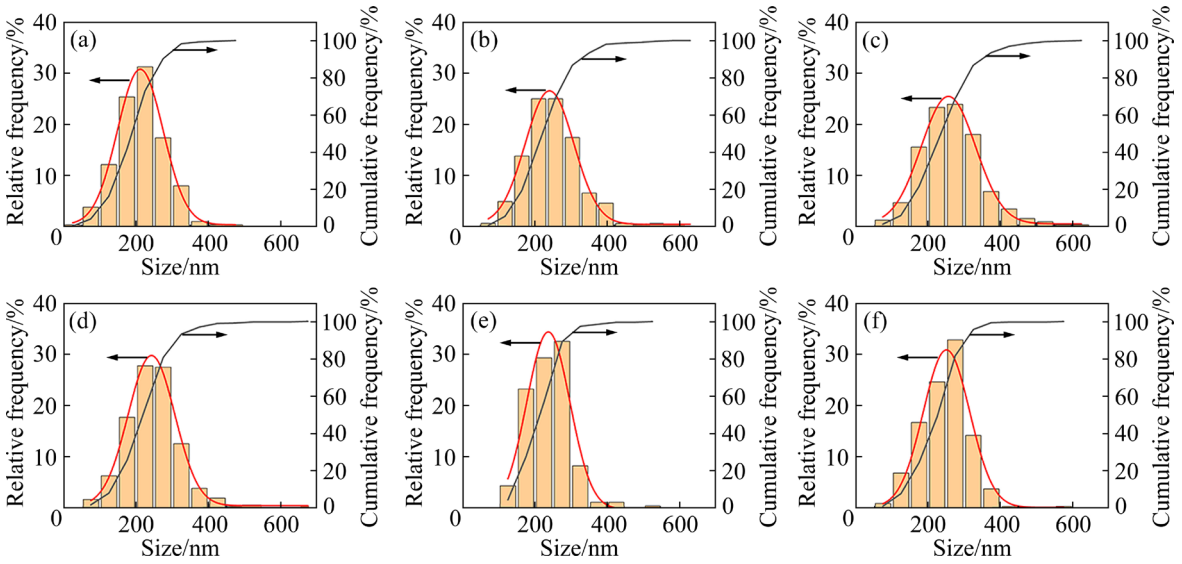

Fig. 7 Size distribution of γ' precipitates after solution treatment (a), and after aging treatment for 5 min at different cooling rates: (b) 25 °C/min; (c) 50 °C/min; (d) 100 °C/min; (e) 125 °C/min, (f) Water cooling

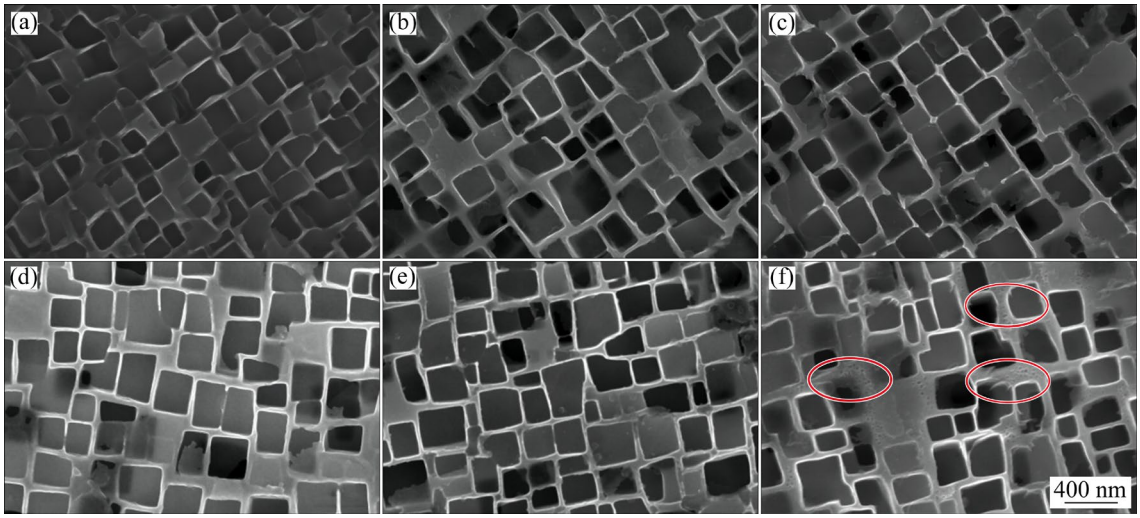

Fig. 8 Morphology of γ' precipitates after solution treatment (a), and after aging treatment for 10 min at different cooling rates: (b) 25 °C/min; (c) 50 °C/min; (d) 100 °C/min; (e) 125 °C/min; (f) Water cooling

element diffusion. In contrast, at higher cooling rates after solution treatment, the microstructure reverts to an unimodal state due to the slow diffusion of elements, with the nucleation rate stabilizing at a relatively constant level. However, as studied in Ref. [30], a bimodal structure still forms even under liquid nitrogen cooling after aging. It means that the high cooling rates may not completely eliminate secondary γ' precipitates, leaving a residual population of fine precipitates that can serve as nuclei for further growth during subsequent aging treatments. Our experiments indicate that secondary γ' precipitation is a distinctive feature of the water-cooled samples, highlighting a competitive dynamic between undercooling and diffusion kinetics. Furthermore, the presence of fine γ' precipitates even at high cooling rates suggests that the transformation process is more complex and requires further investigation.

3.3 Effects of aging time on γ' precipitates

Figure 8 shows the morphological variation of γ' precipitates after solution treatment and after aging treatments for 10 min at different cooling rates. Additionally, Fig. 9 presents the corresponding size distribution for each sample in Fig. 8, with the mean sizes in Table 2. A comparative analysis between Figs. 7 and 9 illustrates a distinct trend: γ' precipitates in samples subjected to aging treatment for 10 min are larger than those aged for 5 min under the same cooling rates. Furthermore, the samples aged for 10 min exhibit a more defined and regular rectangular shape compared to those treated for 5 min.

3.3.1 Size of γ' precipitates

The influence of aging time on γ' precipitation is intricately linked to the diffusion behavior of elements within the alloy [15]. This phenomenon can be quantified through an equation accounting for the size (r) of γ' precipitates as follows:

$$r=\left[\frac{2(C_0-C_{\gamma/\gamma'})}{C_{\gamma'}-C_{\gamma/\gamma'}}\cdot(Dt)\right]^{0.5} \tag{22}$$

where D is the diffusion coefficient of the alloy, and C_0, $C_{\gamma/\gamma'}$ and $C_{\gamma'}$ represent the solute concentrations in the supersaturated γ phase, at the γ/γ' interface, and in the γ' phase, respectively. It suggests that, under certain conditions, time (t) is the only variable parameter affecting the size of the γ' phase. The relationship between the aging time and size of γ' precipitates depends on the element diffusion rate,

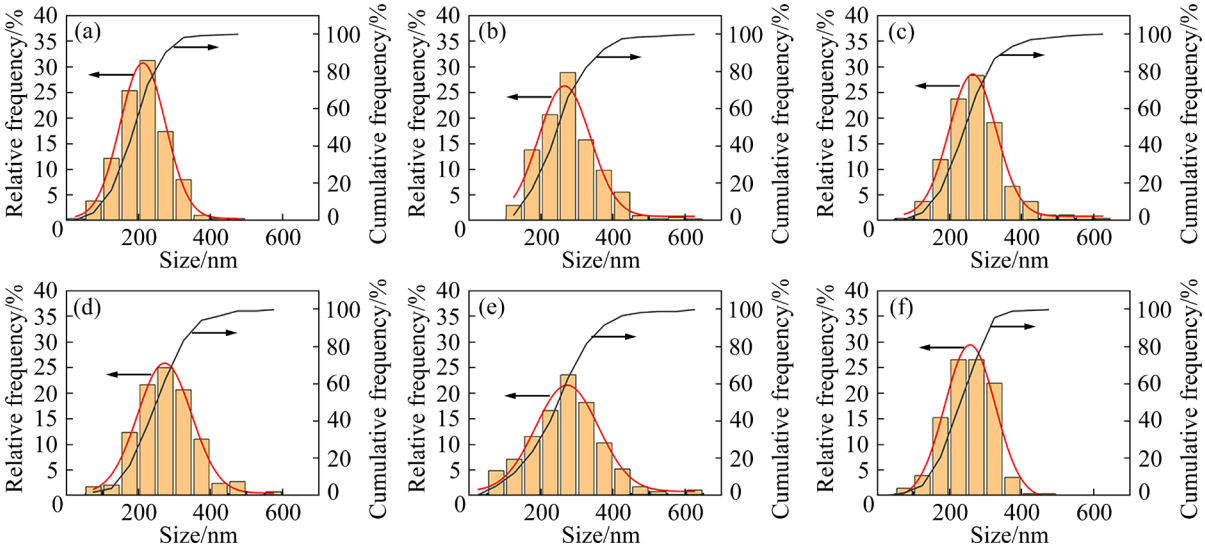

Fig. 9 Size distribution of γ' precipitates after solution treatment (a), and after aging treatment for 10 min at different cooling rates: (b) 25 °C/min; (c) 50 °C/min; (d) 100 °C/min; (e) 125 °C/min; (f) Water cooling

Table 2 Mean size of γ' precipitates after aging treatment for 5 min and 10 min, and cooling at different cooling rates (nm)

Time/min	After solution treatment	After cooling				
		25 °C/min	50 °C/min	100 °C/min	125 °C/min	Water cooling
5	212	257	256	242	237	251
10	212	266	268	270	269	260

which is influenced by various factors such as the diffusion coefficient and the concentrations of solute elements. Consequently, an increase in aging time leads to a proportional increase in the size of γ' precipitates.

3.3.2 Rectangularization of γ' precipitates

Through comparison between Figs. 6 and 8, it was observed that samples with long holding time tended to exhibit a more rectangular morphology. Figure 10 shows the roundness and CDR of both solution-treated and aging samples.

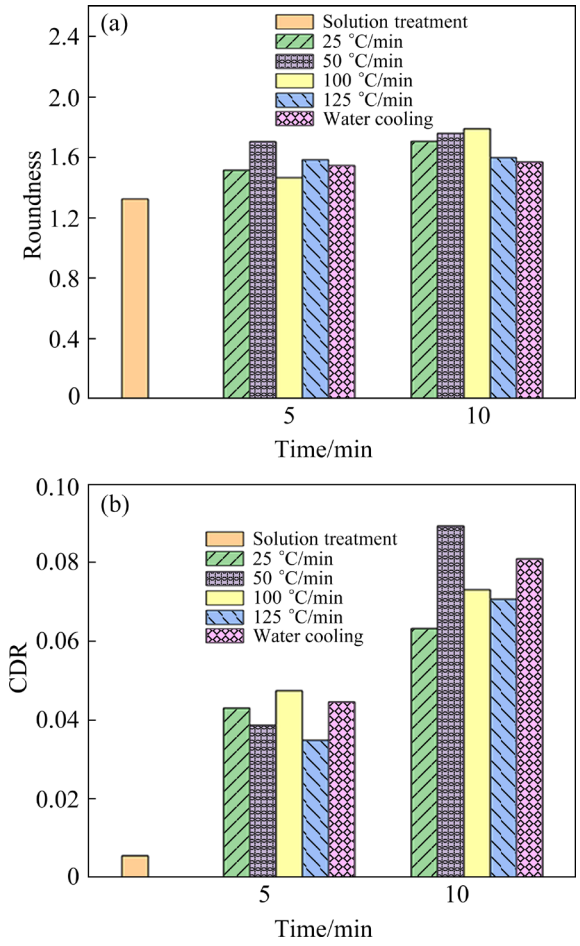

Fig. 10 (a) Roundness of samples treated for different time and at different cooling rates; (b) CDR of each sample

For a perfect circle, its roundness is 1, while for a perfect square, the roundness is 4/π. The further the roundness is from 1, the more pronounced the squareness. However, in the actual precipitation system of nickel-based single-crystal superalloy, the γ' phase is not a perfect square, and it is more appropriate to describe them as rectangles. Furthermore, rectangles with different aspect ratios do not have a fixed roundness. Therefore, roundness may not be a precise indicator in this study. In Fig. 10(a), statistical values of roundness are presented for samples with different holding time and cooling rates. With increasing holding time, there is a trend of roundness deviating from 1, indicating a more rectangular morphology. However, it can be observed that the roundness of the experimental samples is greater than 4/π, which is because the γ' phase in the experimental samples is not a regular cube.

Since roundness cannot precisely describe the morphological changes in our experimental study, we proposed using the CDR. The CDR of each experimental sample is shown in Fig. 10(b). It can be seen that with increasing time, the CDR also shows an increasing trend, indicating that the holding process leads to a more significant rectangularization of the γ' phase.

3.3.3 Phase field simulation of aging process

The above research demonstrates that the γ' phase grows and gradually tends towards a more rectangular shape during aging heat treatment. However, the mechanisms underlying this phenomenon cannot be discerned solely from experimental results. Considering there are few previous studies establishing a quantitative relationship between the degree of γ' phase rectangularization and aging time, our research utilized the phase-field model established in Section 3 to simulate the aging process of DD5 superalloy. Subsequently, the growth of the γ' phase, changes in morphology and size, lattice misfit, and stress distribution during aging will be discussed. The time step in phase field simulation is 1.94×10^3 s. We used 1×10^6 steps to represent the solution-treated state, with aging time denoted as Δt.

Figure 11 illustrates the simulation results depicting the microstructure evolution of the γ' phase at 1100 °C over aging time. It can be observed that the γ' phase gradually grows with increasing time, which is consistent with experimental results shown in Fig. 11(d). Meanwhile, Figs. 12(a) and (b) demonstrate changes in roundness and CDR with respect to holding time. It is worth noting that the γ' phase in the phase-field simulation is cubic, so the roundness metric will not be larger than 4/π. However, the roundness of experimental results, which are most rectangles, is much larger than the

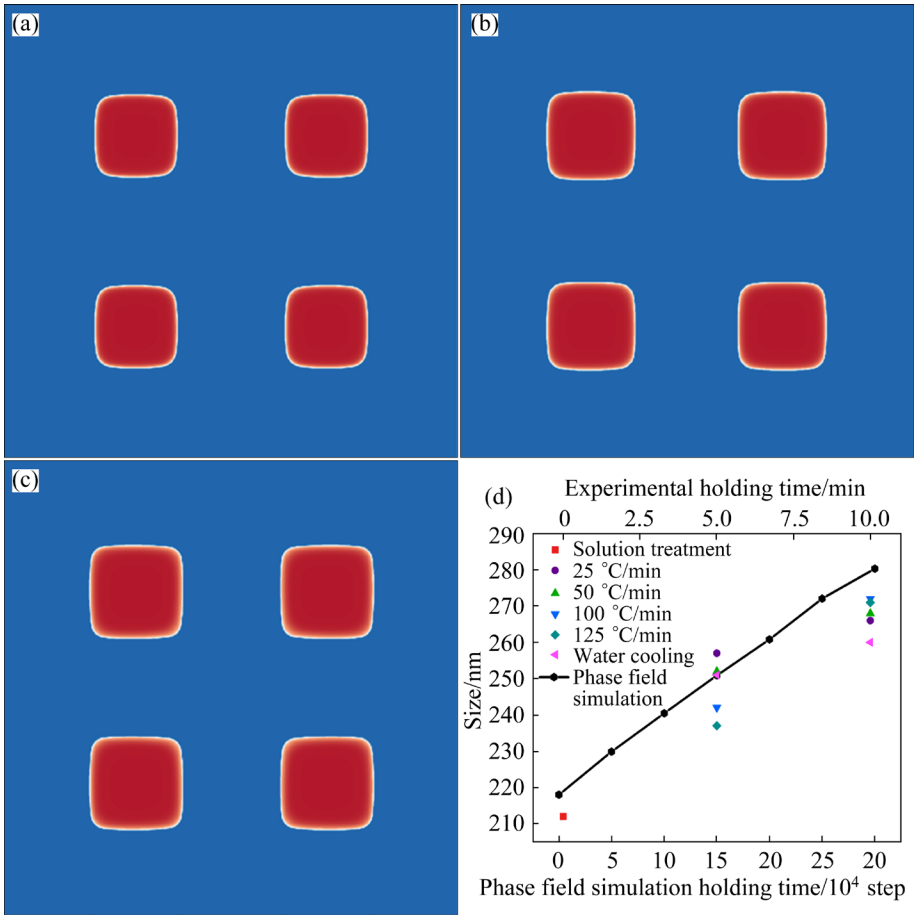

Fig. 11 Microstructure evolution of γ' phase holding at 1100 °C at Δt=0th step (a), Δt=1.5×10^5 steps (b) and 3×10^5 steps (c), and phase field simulation and experimental mean size with time (d)

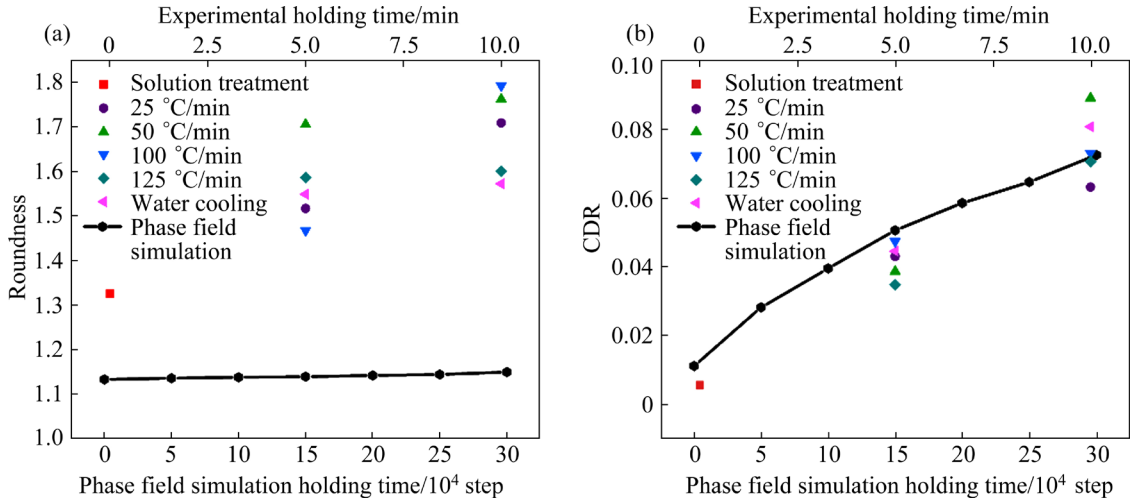

Fig. 12 Phase field simulation and experimental results with time: (a) Roundness; (b) CDR

simulated roundness. This shape difference requires improvement in future phase-field models. Nonetheless, the change trends in CDR over time, obtained from phase-field simulations, align with experimental results, indicating a tendency towards the rectangularization of the precipitated phase.

The lattice misfit δ, calculated by $\delta=\frac{2(a^{\gamma'}-a^{\gamma})}{a^{\gamma'}+a^{\gamma}}$, exhibits a trend, where it starts with a less negative value at the initial stage and increases in absolute value as time progresses, as shown in Fig. 13. This increase signifies an incremental

discrepancy between the lattice constants of the γ matrix and the γ' precipitate: a^{γ} and $a^{\gamma'}$. As reported in Ref. [40], the lattice misfit induces coherency stress, which will lead to a cubic γ' precipitate shape. Consequently, the roundness and CDR depicted in Fig. 12 increase as time progresses.

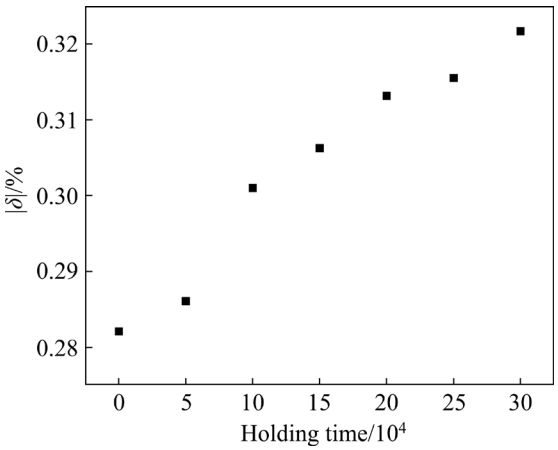

Fig. 13 Phase field simulation of lattice misfit magnitude changes with time

Additionally, Fig. 14 shows the distribution of von Mises stress, hydrostatic pressure, and stress triaxiality at t=1×10^6 steps. The von Mises stress is calculated by $\sigma_{Mises}=\{[(\sigma_1-\sigma_2)^2+(\sigma_2-\sigma_3)^2+(\sigma_1-\sigma_3)^2]/2\}^{1/2}$, reflecting the degree of stress concentration. The hydrostatic pressure is calculated by $\sigma_{Hydrostatic}=(\sigma_1+\sigma_2+\sigma_3)/3$, which reflects the pressure acting uniformly in all directions. The stress triaxiality is calculated by $\sigma_{Triaxiality}=\sigma_{Hydrostatic}/\sigma_{Mises}$, which represents the relative proportion of hydrostatic pressure to von Mises stress and provides insight into the stress state. The observed trends in the distribution of the von Mises stress, hydrostatic pressure, and stress triaxiality along the ⟨111⟩ direction provide valuable insights into the evolving morphology of the precipitated phase. The higher magnitude of von Mises stress along the ⟨111⟩ direction suggests localized stress concentration, indicating regions of intense deformation or strain. Conversely, the relatively low hydrostatic pressure along the same direction implies reduced uniform pressure, potentially facilitating the elongation or stretching of the precipitated phase.

Furthermore, the elevated stress triaxiality along the ⟨111⟩ direction indicates a higher proportion of hydrostatic pressure to von Mises stress, signifying a more isotropic stress state conducive to morphological changes such as rectangularization. Therefore, the concurrent trends of elevated von Mises stress, reduced hydrostatic pressure, and increased stress triaxiality along the ⟨111⟩ direction suggest a mechanical environment that favors the transformation of precipitates towards a more rectangular shape.

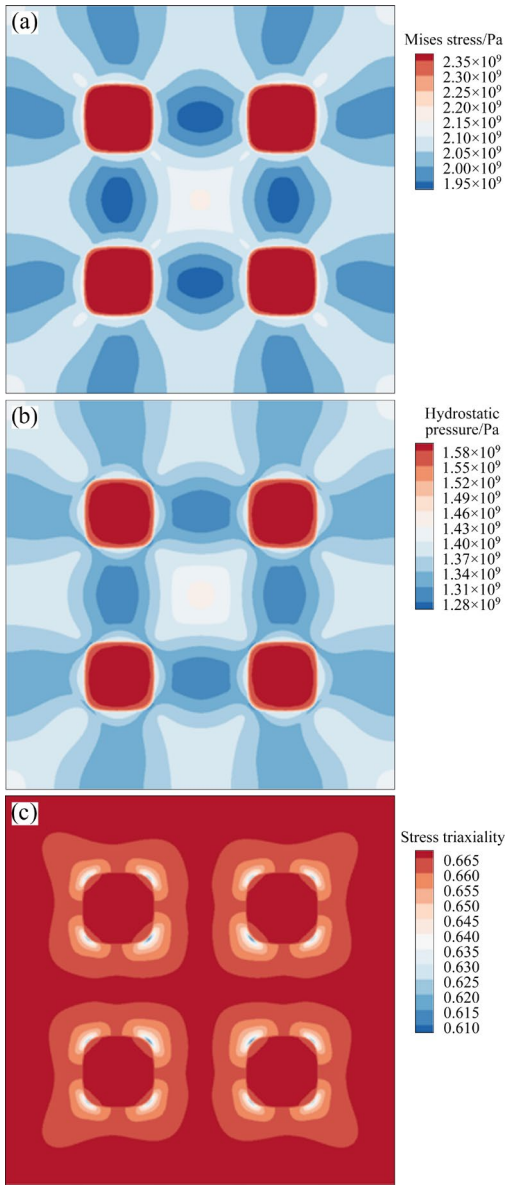

Fig. 14 Stress distribution results at 1×10^6 steps by phase field simulation: (a) von Mises stress; (b) Hydrostatic pressure; (c) Stress triaxiality

The trend of stress triaxiality with increasing aging time is shown in Fig. 15. Figure 15(b) illustrates the evolution of stress triaxiality distribution along line AB over time. Figures 15(c) and (d) depict the evolution of stress triaxiality at Points M and T, respectively. It can be observed that with increasing aging time, the stress triaxiality at

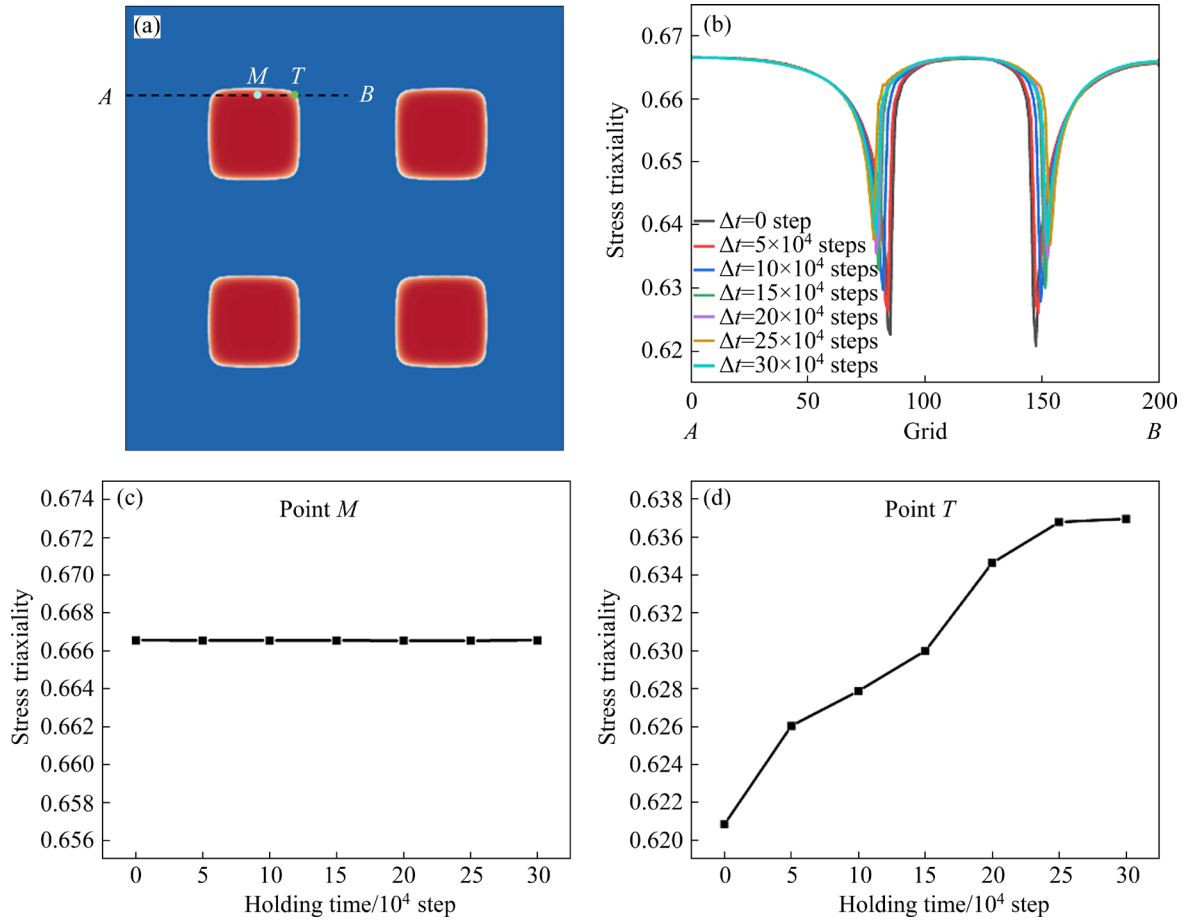

Fig. 15 (a) Schematic diagram of location along Line *AB*, Points *M* and *T*; (b) Stress triaxiality changes with holding time along line *AB* (b), Point *M* (c) and Point *T* (d)

Point *M* (representing the length of the rectangle) remains relatively constant, while the stress triaxiality at Point *T* (representing the vertex of the rectangle) gradually increases. This indicates that, over time, the stress at the vertex of the rectangle becomes more uniformly distributed, contrasting with the initial stage, where it experiences localized stress concentration. This trend suggests a transition to mechanical equilibrium during the rectangularization process, from an initial stage of localized stress concentration to a more uniform stress distribution.

4 Conclusions

(1) Solution treatment effectively reduced eutectic phases, leading to significant dissolution, although some γ' precipitates remained due to high solute concentration.

(2) Secondary γ' precipitates occurred only in samples subjected to water cooling after aging, highlighting the competition between cooling and diffusion.

(3) Samples aged for 5 min at different cooling rates showed larger γ' precipitates than solution-treated ones. Samples aged for 10 min consistently had larger precipitates than those treated for 5 min, regardless of the cooling rate.

(4) The samples treated for 10 min displayed a more regular rectangular shape than those treated for 5 min, indicating the impact of aging duration on γ' morphology.

(5) Phase-field simulations provided insights into γ' growth dynamics, correlating well with experimental observations and showing that coherency stresses and higher stress triaxiality promote the rectangularization of γ' precipitates.

CRediT authorship contribution statement

Ye-yuan HU: Methodology, Conceptualization, Data curation, Writing − Original draft; **Shao-xiang LI:** Investigation, Formal analysis; **Qing-yan XU:** Supervision, Writing − Review & editing.

Declaration of competing interest

The authors declare that they have no known

competing financial interests or personal relationships that could have appeared to influence the work reported in this paper.

Acknowledgments

This work was supported by the Stable Support Project and the Major National Science and Technology Project, China (Nos. 2017-VII-0008-0101, 2017-VI-0003-0073).

References

[1] CHENG Yan, ZHAO Xin-bao, YUE Quan-zhao, PAN Qing-hai, XU Jia-chen, XIA Wan-shun, GU Yue-feng, ZHANG Zhe. The role of Mo on the creep deformation of a 4th generation Ni-based single crystal superalloy at 1100 °C [J]. Materials Today Nano, 2023, 24: 100420.

[2] ZHANG Zhi-wei, CAI Wei, FENG Yi-hui, DUAN Gui-hua, WANG Jing, WANG Jun, YANG Rong, XIAO Pan, KE Fu-jiu, LU Chun-sheng. Dislocation reactions dominated pop-in events in nanoindentation of Ni-based single crystal superalloys [J]. Materials Characterization, 2023, 200: 112883.

[3] LI Xuan-zhe, HAN Chen-xu, YUE Xiao-dai, LI Su-zhi, LI Jia-rong, ZONG Hong-xiang, DING Xiang-dong, SUN Jun. Influence of interfacial dislocation network on strain-rate sensitivity in Ni-based single crystal superalloys [J]. Scripta Materialia, 2024, 240: 115838.

[4] WANG Heng-zhe, LONG Hai-bo, LIU Yi-nong, ZHAO Yun-song, LI Xue-qiao, YANG Guo, YANG Xiao-meng, CHEN Yan-hui, MAO Sheng-cheng, ZHANG Ze, HAN Xiao-dong. The widening of the solution heat treatment window by the addition of Ru in Ni-based single crystal superalloy [J]. Materials Characterization, 2023, 203: 113057.

[5] TAN Ke-jie, WANG Xin-guang, LIANG Jing-jing, MENG Jie, ZHOU Yi-zhou, SUN Xiao-feng. Effects of rejuvenation heat treatment on microstructure and creep property of a Ni-based single crystal superalloy [J]. Journal of Materials Science & Technology, 2021, 60: 206−215.

[6] LATIEF F H, KAKEHI K. Influence of heat treatment on anisotropic creep behavior of aluminide coating on a Ni-base single crystal superalloy [J]. Materials & Design, 2013, 52: 134−142.

[7] KHAN T, CARON P. Effect of processing conditions and heat treatments on mechanical properties of single-crystal superalloy CMSX-2 [J]. Materials Science and Technology, 1986, 2(5): 486−492.

[8] RU Yi, LI Shu-suo, PEI Yan-ling, ZHOU Jian, GONG Sheng-kai, XU Hui-bin. Interdendritic Mo homogenization and sub-solidus melting during solution treatment in the Mo-strengthening single crystal superalloys [J]. Journal of Alloys and Compounds, 2016, 662: 431−435.

[9] CHENG Tian-wei, WANG Yan, ZHAO Yun-xing, LV Liang-xing, HU Qing, MA De-xin. Effect of remelting solution heat treatment on microstructure evolution of nickel-based single crystal superalloy DD5 [J]. Materials Characterization, 2022, 192: 112186.

[10] HU Ming-hao, LI Chong, GUO Qian-ying, HAN Xiao-jun, DING Ran, LI Hui-jun, XIA Xing-chuan, LIU Yong-chang. Improving creep property and deformation mechanism of transient liquid phase bonded polycrystalline Ni3Al-based superalloy with post bond heat treatment [J]. Materials Science and Engineering: A, 2023, 874: 145078.

[11] RUSTAMOV I, CHENG Yong-jun, KANIEV D, WANG Bi, XIANG Le-hong, SABIROVA O, WANG Yu-ming, WANG Zi-xi. Triple heat treatment effects of Inconel X-750 superalloy on its microstructure, hardness, and high-temperature fretting wear characteristics [J]. Wear, 2023, 534/535: 205128.

[12] WANG Yuan-chen, LEI Li-ming, SHI Lei, LIANG Fei, WAN Hong-yuan, ZHANG Bin, ZHANG Guang-ping. Effect of heat treatment on strain hardening ability of selective laser melted precipitation-hardened GH4169 superalloy [J]. Materials Characterization, 2022, 190: 112064.

[13] van der MOLEN E H, OBLAK J M, KRIEGE O H. Control of γ' particle size and volume fraction in the high temperature superalloy Udimet 700 [J]. Metallurgical Transactions, 1971, 2: 1627−1633.

[14] WANG Fu, MA De-xin, ZHANG Jun, LIU Lin, BOGNER S, BÜHRIG-POLACZEK P A. Effect of local cooling rates on the microstructures of single crystal CMSX-6 superalloy: A comparative assessment of the Bridgman and the downward directional solidification processes [J]. Journal of Alloys and Compounds, 2014, 616: 102−109.

[15] YUE Xiao-dai, LI Jia-rong, WANG Xin-guang. The microstructure of a single crystal superalloy after different aging heat treatments [J]. Rare Metals, 2018, 37: 210−216.

[16] YANG Xi-xi, CUI Xue, YUAN Huang. Correlations between microstructure evolution and mechanical behavior of a nickel-based single crystal superalloy with long-term aging effects [J]. Materials Characterization, 2020, 169: 110652.

[17] FUCHS G E. Solution heat treatment response of a third generation single crystal Ni-base superalloy [J]. Materials Science and Engineering: A, 2001, 300(1/2): 52−60.

[18] CUI Ren-jie, HUANG Zhao-hui. Microstructural evolution and stability of second generation single crystal nickel-based superalloy DD5 [J]. Transactions of Nonferrous Metals Society of China, 2016, 26(8): 2079−2085.

[19] AI Cheng, XI Li-guo, WANG Bo, SUN Yang-hui, ZHANG Jun, SU Hai-jun, YANG Wen-chao, LIU Lin, SUN Zhi-ping, CHEN Yong-nan. Investigation on solution heat treatment response and γ' solvus temperature of a Mo-rich second generation Ni based single crystal superalloy [J]. Intermetallics, 2020, 125: 106896.

[20] HEGDE S R, KEARSEY R M, BEDDOES J C. Designing homogenization–solution heat treatments for single crystal superalloys [J]. Materials Science and Engineering: A, 2010, 527(21/22): 5528−5538.

[21] LV Jin-juan. Heat treatment optimization and high temperature performance of nickel-base single crystal superalloy DD5 [D]. Zhenjiang: Jiangsu University. 2019. (in Chinese)

[22] ZHANG Yan-bin, LIU Lin, HUANG Tai-wen, YUE Quan-zhao, SUN De-jian, ZHANG Jun, YANG Wen-chao, SU Hai-jun, FU Heng-zhi. Investigation on a ramp solution heat

treatment for a third generation nickel-based single crystal superalloy [J]. Journal of Alloys and Compounds, 2017, 723: 922−929.

[23] WANG Xin, MA Shi-cheng, HU Dian-yin, XU Chun-ling, LUO Xue-kun, TANG Zhi-hui. Effect of aging temperature on the fatigue properties of shot-peened single crystal superalloy at intermediate temperature [J]. International Journal of Fatigue, 2022, 156: 106675.

[24] ALIAKBARI-SANI S, VAFAEENEZHAD H, ARABI H, EBRAHIMI G R. Quantitative kinetic analysis of γ′ precipitate evolution in a Co−Al−W superalloy during aging heat treatment [J]. Journal of Materials Research and Technology, 2022, 21: 3425−3439.

[25] WEI Li, ZHANG Zhi-gang, ZHANG Heng, LI Shu-suo, GONG Sheng-kai. Influence of aging heat treatment on microstructure and hardness of single crystal Ni3Al-base superalloy IC21 [J]. Procedia Engineering, 2012, 27: 1081−1088.

[26] XU J H, SCHULZ F, PENG R L, HRYHA E, MOVERARE J. Effect of heat treatment on the microstructure characteristics and microhardness of a novel γ′ nickel-based superalloy by laser powder bed fusion [J]. Results in Materials, 2021, 12: 100232.

[27] HE Xin, LIU Chang, YANG Yi-kai, DING Jian, CHEN Xue-guang, XIA Xing-chuan, TANG Ying, LIU Yong-chang. Directional coarsening behavior of primary γ′ phase in Ni3Al-based superalloy during aging heat treatment [J]. Journal of Alloys and Compounds, 2021, 872: 159674.

[28] XU Jia-chen, ZHAO Xin-bao, YUE Quan-zhao, XIA Wan-shun, DUAN Huan-chang, GU Yue-feng, ZHANG Ze. A morphological control strategy of γ′ precipitates in nickel-based single-crystal superalloys: An aging design, fundamental principle, and evolutionary simulation [J]. Materials Today Nano, 2023, 22: 100335.

[29] QU Peng-fei, YANG Wen-chao, QIN Jia-run, LIU Chen, DUAN Xing-yu, ZHANG Jun, LIU Lin. Determining the precipitation temperature of secondary γ′ phases by remelting method in Ni-based single crystal superalloys [J]. Intermetallics, 2023, 162: 108017.

[30] XIA Wan-shun, ZHAO Xin-bao, WANG Jiang-wei, YUE Quan-zhao, CHENG Yuan, KONG Ling-yi, ZHANG Yue-fei, GU Yue-feng, BEI Hong-bin, ZHANG Ze. New strategy to improve the overall performance of single-crystal superalloys by designing a bimodal γ′ precipitation microstructure [J]. Acta Materialia, 2023, 257: 119200.

[31] HUANG Hai-liang, ZHANG Hong-fei, HU Ben-fu, WANG Hao, LIU Guo-quan. Study on γ′ precipitation behavior in a nickel-based PM superalloy during interrupted continuous cooling [J]. Intermetallics, 2020, 116: 106659.

[32] YANG Min, ZHANG Jun, WEI Hua, GUI Wei-min, SU Hai-jun, JIN Tao, LIU Lin. Influence of cooling rate on the formation of bimodal microstructures in nickel-base superalloys during continuous two-step aging [J]. Computational Materials Science, 2018, 149: 14−20.

[33] XU Qing-yan, ZHANG Ya-qian. Precipitation and growth simulation of γ′ phase in single crystal superalloy DD6 with multiphase-field method and explicit nucleation algorithm [J]. Metals, 2020, 10: 1346.

[34] STEINBACH I, APEL M. Multi phase field model for solid state transformation with elastic strain [J]. Physica D: Nonlinear Phenomena, 2006, 217: 153−160.Cc

[35] REUSS A. Calculation of the yield point of mixed crystals based on the plasticity condition for single crystals[J]. Journal of Applied Mathematics and Mechanics, 1929, 9(1): 49−58. (in German)

[36] HILL R. Elastic properties of reinforced solids: Some theoretical principles [J]. Journal of the Mechanics and Physics of Solids, 1963, 11(5): 357−372.

[37] GINZBURG V L, LANDAU L D. On the theory of superconductivity [M]// On Superconductivity and Superfluidity. Berlin, Heidelberg: Springer, 2008: 113−137.

[38] CAHN J W, HILLIARD J E. Free energy of a nonuniform system. I: Interfacial free energy [J]. The Journal of Chemical Physics, 1958, 28: 258−267.

[39] EIKEN J, BÖTTGER B, STEINBACH I. Multiphase-field approach for multicomponent alloys with extrapolation scheme for numerical application [J]. Phys Rev E, 2006, 73: 066122. (in German)

[40] YANG Cong, XU Qing-yan, LIU Bai-cheng. A high precision extrapolation method in multiphase-field model for simulating dendrite growth [J]. Journal of Crystal Growth, 2018, 490: 25−34.

[41] GUO W, STEINBACH I, SOMSEN C, EGGELER G. On the effect of superimposed external stresses on the nucleation and growth of Ni_4Ti_3 particles: A parametric phase field study [J]. Acta Materialia, 2011, 59: 3287−3296.

[42] MICHEL J C, MOULINEC H, SUQUET P. Effective properties of composite materials with periodic microstructure: A computational approach [J]. Computer Methods in Applied Mechanics and Engineering, 1999, 172: 109−143.

[43] NEUMEIER S, PYCZAK F, GÖKEN M. The temperature dependent lattice misfit of rhenium and ruthenium containing nickel-base superalloys−Experiment and modelling [J]. Materials & Design, 2021, 198: 109362.

[44] MIAO Zhu-jun, SHAN Ai-dang, WU Yuan-biao, LU Jun, XU Wen-liang, SONG Hong-wei. Quantitative analysis of homogenization treatment of INCONEL718 superalloy [J]. Transactions of Nonferrous Metals Society of China, 2011, 21: 1009−1017.

[45] PRADELL T, CRESPO D, CLAVAGUERA N, CLAVAGUERA-MORA M T. Diffusion controlled grain growth in primary crystallization: Avrami exponents revisited [J]. Journal of Physics: Condensed Matter, 1998, 10: 3833−3844.

[46] ASTA M, BECKERMANN C, KARMA A, KURZ W, NAPOLITANO R, PLAPP M, PURDY G, RAPPAZ M, TRIVEDI R. Solidification microstructures and solid-state parallels: Recent developments, future directions [J]. Acta Materialia, 2009, 57: 941−971.

镍基单晶高温合金时效过程中γ′相的形态与尺寸演变

胡业媛，李少翔，许庆彦

清华大学 材料学院 先进材料加工技术教育部重点实验室，北京 100084

摘　要：采用多阶段固溶工艺处理镍基单晶高温合金，随后采用不同时效时间和冷却速率进行调控。利用扫描电子显微镜(SEM)对合金的显微组织进行表征，观察γ′相的形貌特征。此外，采用相场方法模拟了时效过程中γ′相的生长，并分析其形貌演变。实验结果表明，多阶段固溶处理工艺有效消除了共晶相和碳化物。此外，与时效时间为 5 min 的样品相比，时效 10 min 的样品中的γ′相更大且更矩形化。值得注意的是，在水冷条件下的样品中观察到了二次γ′析出相。提出了两个量化γ′相矩形化程度的指标，并得到了有效应用。基于模拟结果，晶格错配引起的相干应力和沿⟨111⟩方向的应力三轴度导致了γ′相的矩形化。

关键词：镍基高温合金；时效保温时间；γ′相矩形化；相场模拟

(Edited by Xiang-qun LI)